An ALMA 1.3 millimeter search for debris disks around solar-type stars in the Pleiades

Sullivan, Devin; Wilner, David J.; Matrà, Luca; Wyatt, Mark C.; Andrews, Sean M.; MacGregor, Meredith A.; Matthews, Brenda

Publisher's version / Version de l'éditeur:
https://doi.org/10.3847/1538-3881/ac80c5
The Astronomical Journal, 164, 3, 2022-08-18

The Astronomical Journal, 164:100 (13pp), 2022 September https://doi.org/10.3847/1538-3881/ac80c5

An ALMA 1.3 millimeter Search for Debris Disks around Solar-type Stars in the Pleiades

Devin Sullivan[1], David J. Wilner[1], Luca Matrà[2,3], Mark C. Wyatt[4], Sean M. Andrews[1], Meredith A. MacGregor[5], and Brenda Matthews[6]

[1] Center for Astrophysics | Harvard & Smithsonian, 60 Garden St., Cambridge, MA 02138, USA; dwilner@cfa.harvard.edu
[2] School of Physics, Trinity College Dublin, The University of Dublin, College Green, Dublin 2, Ireland
[3] Centre for Astronomy, School of Physics, National University of Ireland Galway, University Road, Galway, H91 TK33, Ireland
[4] Institute of Astronomy, University of Cambridge, Madingley Road, Cambridge CB3 0HA, UK
[5] Department of Astrophysical and Planetary Sciences, University of Colorado, 2000 Colorado Avenue, Boulder, CO 80309, USA
[6] Herzberg Astronomy & Astrophysics Research Centre, National Research Council of Canada, 5071 West Saanich Road, Victoria, BC V9E 2E7, Canada
Received 2022 March 23; revised 2022 June 23; accepted 2022 July 11; published 2022 August 18

Abstract

Millimeter emission from debris disks around stars of different ages provides constraints on the collisional evolution of planetesimals. We present ALMA 1.3 millimeter observations of a sample of 76 Solar-type stars in the ∼115 Myr old Pleiades star cluster. These ALMA observations complement previous infrared observations of this sample by providing sensitivity to emission from circumstellar dust at lower temperatures, corresponding to debris at radii comparable to the Kuiper Belt and beyond. The observations obtain a beam size of 1.″5 (200 au) and a median rms noise of 54 μJy beam^{-1}, which corresponds to a fractional luminosity $L_{\rm dust}/L_{\rm star} \sim 10^{-4}$ for 40 K dust for a typical star in the sample. The ALMA images show no significant detections of the targeted stars. We interpret these limits in the context of a steady-state collisional cascade model for debris disk evolution that provides a good description of observations of the field population near the Sun but is not well-calibrated on younger populations. The ALMA nondetections of the Pleiades systems are compatible with the disk flux predictions of this model. We find no high fractional luminosity outliers from these ALMA data that could be associated with enhanced collisions resulting from activity not accounted for by steady-state evolution. However, we note that two systems (H II 1132 and HD 22680) show 24 μm excess much higher than the predictions of this model, perhaps due to unusually high dust production from dynamical events involving planets.

Unified Astronomy Thesaurus concepts: Debris disks (363); Star clusters (1160)

1. Introduction

The collisions between planetesimals orbiting main-sequence stars produce dust heated by stellar radiation that is manifested as debris disk emission. Debris disk detection statistics together with trends of dust excess with stellar age probe the evolution of planetesimal belts, which may be influenced by planets (see reviews by Wyatt 2008; Matthews et al. 2014; Hughes et al. 2018). Studies of 24 and 70 μm dust emission around stars with a range of ages and spectral types show that debris disk detection frequency and fractional luminosity ($L_{\rm dust}/L_{\rm star}$) rise over perhaps 10 s of Myr and then decline slowly over 100 s of Myr (Rieke et al. 2005; Su et al. 2006; Carpenter et al. 2009). These data can be explained in a theoretical framework that invokes an early phase of runaway growth and merging of planetesimals (Kenyon & Bromley 2008) followed by a steady-state destructive collisional cascade (Dominik & Decin 2003). In this picture, planetesimals collide and fragment into smaller objects that in turn collide and fragment, ending in circumstellar dust small enough to be removed by stellar winds and radiation. Because collisional depletion is faster for smaller disks and more massive disks, the wide dispersion of fractional luminosity and dust temperature observed at a given age may be accounted for by variations in the initial planetesimal belt masses and radii (Wyatt et al. 2007a; Löhne et al. 2008). This standard collisional evolution model for debris disks predicts a maximum fractional luminosity of 10^{-3} at early times, in line with the most extreme systems known (Wyatt et al. 2007b).

Observational constraints on evolutionary models are conspicuously sparse for debris disks around Solar-type stars at large radii, beyond 10 au, for ages near 100 Myr, i.e., older than nearby moving groups, but younger than the nearby field. This is a critical epoch when young planetary systems may be dynamically active. Such systems are especially relevant to provide context for the evolution of our Kuiper Belt, which apparently was destabilized by the outward migration of Neptune and underwent a dramatic dynamical depletion, from an initial mass of more than 10 $M_\oplus$ at radii 30–50 au, to less than 0.1 $M_\oplus$ today; modeling suggests that the corresponding fractional luminosity decreased from 10^{-3} to 10^{-7} (Booth et al. 2009). This is also the epoch of the formation of the Earth's moon (e.g., see review by Asphaug 2014). Sensitive surveys of the (older) field population of Solar-type stars (FGK type) within 20 pc show the occasional system (5 of 275) with debris at large radii and high fractional luminosity ($>5 \times 10^{-5}$) whose presence is not predicted by standard steady-state collisional evolution models (Sibthorpe et al. 2018). A plausible hypothesis for such large excess is an ongoing system-wide dynamical event involving planets, akin to the one that shaped the Kuiper Belt. Another possibility is that these systems follow the "late bloomer" path revealed by coagulation models, where protoplanetary disk rings with nearly completely efficient planetesimal formation slowly rise to these high fractional luminosities over ∼1 Gyr (Najita et al. 2022).

The Pleiades cluster has long provided a benchmark for debris disk evolution studies because of its combination of (1)

age: 115 ± 10 Myr (Stauffer et al. 1998), the epoch of maximum dust production rate in "self-stirred" evolutionary models (Kenyon & Bromley 2008); (2) proximity: 133.5 ± 1.2 pc (Melis et al. 2014; Gaia Collaboration et al. 2018), for maximum sensitivity; and (3) a sufficiently large sample: $\mathcal{O}(100)$ Solar-type stars, to obtain meaningful statistics to compare with evolutionary models. No other star cluster satisfies these criteria. Sensitive searches for warm (>100 K) circumstellar dust in the Pleiades were performed in a series of Spitzer 24 μm surveys that include members of spectral type F5 to K1 (Stauffer et al. 2005; Gorlova et al. 2006; Sierchio et al. 2010). For systems observed at 24 μm, 23/71 (32%) show excesses greater than 10% above the photospheres, attributed to dusty debris at blackbody radii from $\sim$1 to 10 au. By comparison, only 3/164 (2%) of the Solar-type stars in the 750 Myr old Praesepe cluster (mean distance 187.3 pc; Lodieu et al. 2019) show 24 μm excesses, as dust production declines with time due to collisional depletion in the inner regions (e.g., Gáspár et al. 2009). All models that explain debris disk evolution predict that the Pleiades should harbor a population of colder (<100 K) debris belts at larger radii (>10 au).

There are few existing constraints on cold dust belts in the Pleiades. Emission at 24 μm is on the Wien side of the spectral peak for dust at radii of 10s of au and therefore exponentially depressed. A subset of 20 Pleiades systems was observed by Spitzer at 70 μm as a part of the FEPS program, which targeted 328 Solar-type stars spanning ages of 3 Myr to 3 Gyr to study debris disk evolution (Carpenter et al. 2009). No excess emission was detected from these 20 Pleiades targets at 70 μm, but with only marginal sensitivity to the outer belts of interest (Stauffer et al. 2005). Millimeter wavelengths provide direct access to cold dust, but millimeter observations of the Pleiades have yet to reach relevant levels of sensitivity to $L_{\rm dust}/L_{\rm star}$ (Zuckerman & Becklin 1993; Greaves et al. 2009; Roccatagliata et al. 2009).

The Survey of Nearby Stars with the JCMT provided 0.85 (and 0.45) millimeter follow up of debris disks near the Sun known from far-infrared surveys, resulting in 31 detections of FGK stars (Holland et al. 2017). Nearly all systems with ages <50 Myr were detected, with lower detection rates at older ages, in line with expectations for collisional evolution. Only six systems with ages in the range 50–200 Myr were detected. Now, the unprecendented sensitivity of ALMA allows for unbiased surveys of millimeter emission from circumstellar to constrain debris disk evolutionary models. For example, Lovell et al. (2021) used ALMA to detect 4/30 Class III systems in the Lupus clouds and concluded that the debris belts found around older stars are already present at an age of $\sim$2 Myr.

In this paper, we report the results of an ALMA survey of Solar-type stars in the Pleiades cluster at 1.3 millimeters wavelength. These observations improve on previous millimeter observations by about an order of magnitude in sensitivity and for a much larger sample, and they complement previous infrared observations of the same stars. In Section 2, we describe the details of the ALMA observations. In Section 3, we present the results for the sample. In Section 4, we discuss these results in the framework of steady-state collisional evolution developed by Wyatt & Dent (2002) and previously applied to Solar-type stars by Kains et al. (2011) and Sibthorpe et al. (2018). Finally, Section 5 summarizes the conclusions from this study.

2. Observations

2.1. ALMA Sample Selection

We based the ALMA survey targets on the sample of 76 Solar-type Pleiades stars with reliable 24 μm photometry compiled by Sierchio et al. (2010).[7] The sample was derived from the work of Stauffer et al. (2005) that determined each star to be a likely Pleiades cluster member based on radial velocities, proper motions, chromospheric and coronal activity indicators, and lithium abundance. These stars have colors $1.5 < V - K_S < 2.15$, corresponding to spectral types F5 to K1. None of the stars in this sample shows evidence for hot (>300 K) dust, from stringent limits of excess emission at wavelengths $\lesssim$8 μm. This is consistent with the expected clearing of inner disk regions (<1 au) by collisions over $\sim$100 Myr (and perhaps also by planets). Table 1 lists the target stars and their coordinates, together with the stellar effective temperatures and luminosities from the analysis provided in the Gaia DR2 catalog (Gaia Collaboration et al. 2018), where available Table 1 also lists estimates of the stellar mass based on the luminosity-mass relation of Demircan & Kahraman (1991) for zero-age main-sequence stars in this mass range. The last column lists the 24 μm excess ratio ($F_{\rm obs}/F_{\rm star}$) determined by Sierchio et al. (2010), with significant detections of circumstellar dust emission indicated in bold(excess ratio >1.1, i.e., exceeding 3σ). The 20 systems observed at 70 μm by Stauffer et al. (2005) are at the end of Table 1 (demarcated by a line).

2.2. ALMA Parameters and Observations

The ALMA Band 6 (1.3 mm) observations were performed in 7 execution blocks in the period from 2019 December 12 to 2019 December 18 with 42 to 44 available antennas (program 2019.1.00251.S). The array was in configuration C43-2, which provided a beam size of $\sim 1\farcs5$ (200 au) and $12''$ (1600 au) maximum recoverable scale. Each star was observed for 4.2 minutes. The correlator setup included three spectral windows centered at 232.5, 247.0, and 245.0 GHz with 2.0 GHz bandwidth and 128 channels (TDM mode), and one spectral window centered at 230.538 GHz with 1.875 GHz bandwidth and 3840 channels (FDM mode). The field of view was set by the $27''$ (FWHM) primary beam of the ALMA antennas at 1.3 mm. The data sets were processed by the ALMA standard calibration pipeline using the Common Astronomy Software Applications (CASA) software package (version 5.6.1; McMullin et al. 2007). Table 2 presents a log of the ALMA observations. In brief, the time dependence of phase and amplitude were calibrated with frequent observations of the nearby quasar J0357+2319, the passband response was calibrated with observations of the strong source J04323–0120, and the absolute flux scale was referenced to ALMA observations of Solar System objects with an estimated accuracy of 10%.

2.3. ALMA Sensitivity in Context

A useful way to contextualize the sensitivity of these ALMA observations is to compare detection limits from surveys at different wavelengths in terms of fractional luminosity, which

[7] We note two modifications of the ALMA sample from the compilation of Sierchio et al. (2010): AK 1B 146 (HD 23170, H II 177) was not included as it is not a Pleiades member (Torres et al. 2021), and H II 1776 was included as it was in the FEPS sample observed at 70 μm by Stauffer et al. (2005).

Table 1
ALMA Pleiades Targets

Name	Alternate Name	R.A. (J2000)	Decl (J2000)	Distance[a] (pc)	$T_{\rm eff}$[b] (K)	$L_{\rm star}$[b] ($L_\odot$)	$M_\star$ ($M_\odot$)	24 μm excess ratio[c]
HIP 17317	AK IA 36	3:42:24.05	22:25:15.2	$137.4^{+1.0}_{-1.0}$	5626^{+101}_{-113}	$1.19^{+0.01}_{-0.01}$	1.04	1.03
BD+21 508	AK IA 56	3:43:31.15	22:09:29.2	$135.0^{+1.2}_{-1.1}$	5468^{+379}_{-123}	$1.14^{+0.01}_{-0.01}$	1.03	1.13
HD 23312	AK IA 76	3:44:58.94	22:01:56.0	$141.1^{+1.2}_{-1.2}$	6253^{+134}_{-147}	$2.66^{+0.03}_{-0.03}$	1.32	**1.26**
HD 24463	AK IA 317	3:54:21.62	24:04:31.6	$135.3^{+1.0}_{-1.0}$	6136^{+201}_{-190}	$1.97^{+0.02}_{-0.02}$	1.21	1.01
HD 22627	AK IB 7	3:39:09.15	24:22:03.3	$143.2^{+1.0}_{-1.0}$	5924^{+81}_{-92}	$2.01^{+0.02}_{-0.02}$	1.22	**1.12**
HIP 17044	AK IB 8	3:39:13.51	24:27:58.6	$141.7^{+0.9}_{-0.9}$	5733^{+181}_{-761}	$1.24^{+0.01}_{-0.01}$	1.06	1.04
HD 23598	AK IB 365	3:47:20.91	25:31:32.1	$136.2^{+1.0}_{-0.9}$	5892^{+113}_{-266}	$1.84^{+0.02}_{-0.02}$	1.18	1.01
HD 24086	AK IB 590	3:51:06.36	25:35:40.0	$139.0^{+1.3}_{-1.3}$	6430^{+270}_{-149}	$3.55^{+0.04}_{-0.04}$	1.44	0.99
HD 23975	AK IB 560	3:50:17.70	25:22:45.5	$137.3^{+1.3}_{-1.2}$	6155^{+283}_{-212}	$2.17^{+0.03}_{-0.03}$	1.24	**1.34**
HD 22444	AK II 34	3:37:24.07	22:21:02.6	$132.3^{+1.6}_{-1.5}$	6135^{+102}_{-101}	$3.04^{+0.04}_{-0.04}$	1.37	1.06
TYC 1798-465-1	AK II 359	3:37:34.93	24:14:10.8	$155.4^{+1.2}_{-1.2}$	5713^{+156}_{-252}	$1.21^{+0.01}_{-0.01}$	1.05	0.99
HIP 16979	AK II 383	3:38:22.61	22:29:58.0	$137.4^{+0.9}_{-0.9}$	5880^{+118}_{-129}	$1.50^{+0.01}_{-0.01}$	1.12	**1.12**
HD 22680	AK II 437	3:39:41.22	23:17:26.3	$140.5^{+1.1}_{-1.1}$	6057^{+181}_{-217}	$1.75^{+0.02}_{-0.02}$	1.17	**3.79**
HIP 16639	AK III 288	3:34:07.34	24:20:39.1	$137.2^{+0.9}_{-0.9}$	6086^{+160}_{-171}	$2.36^{+0.02}_{-0.02}$	1.27	0.99
H II 25	HD 23061	3:42:55.15	24:29:34.2	$138.4^{+1.0}_{-1.0}$	6197^{+464}_{-137}	$2.54^{+0.02}_{-0.02}$	1.30	**1.12**
H II 102	TYC 1799-118-1	3:43:24.56	23:13:32.5	$138.8^{+0.7}_{-0.7}$	5338^{+529}_{-60}	$1.09^{+0.01}_{-0.01}$	1.02	1.04
H II 1132	HD 23514	3:46:38.43	22:55:10.4	$138.2^{+1.0}_{-1.0}$	6269^{+392}_{-196}	$2.68^{+0.03}_{-0.03}$	1.32	**17.44**
H II 1139	HD 23513	3:46:40.02	23:06:36.3	$137.2^{+1.1}_{-1.1}$	6365^{+179}_{-150}	$2.67^{+0.03}_{-0.03}$	1.32	1.09
H II 1766	HD 23732	3:48:16.91	25:12:53.6	$137.8^{+1.5}_{-1.4}$	6614^{+430}_{-336}	$3.19^{+0.04}_{-0.04}$	1.39	**1.60**
H II 2172	HD 282965	3:49:11.77	24:38:10.9	$139.1^{+1.1}_{-1.1}$	5809^{+50}_{-190}	$1.10^{+0.01}_{-0.01}$	1.02	**1.10**
H II 3031	HD 24132	3:51:27.25	24:31:06.2	$135.9^{+1.2}_{-1.2}$	6753^{+239}_{-201}	$4.25^{+0.05}_{-0.05}$	1.51	1.01
TYC 1802-95-1	PELS 7	3:34:47.23	26:05:40.3	$177.2^{+1.8}_{-1.7}$	5596^{+163}_{-105}	$1.79^{+0.02}_{-0.02}$	1.18	0.99
HIP 17020	PELS 20	3:38:56.90	24:34:10.4	$139.1^{+1.3}_{-1.3}$	5723^{+127}_{-170}	$1.02^{+0.01}_{-0.01}$	1.00	**1.19**
HIP 17245	PELS 23	3:41:36.19	25:37:08.6	$138.5^{+1.0}_{-1.0}$	5800^{+124}_{-175}	$1.54^{+0.01}_{-0.01}$	1.12	1.06
HIP 17125	PELS 25	3:40:03.11	27:44:24.9	$138.8^{+2.6}_{-2.5}$	6220^{+95}_{-133}	$2.26^{+0.05}_{-0.05}$	1.26	1.02
BD+21 516	PELS 40	3:45:09.91	21:42:15.5	$127.3^{+0.8}_{-0.8}$	5837^{+267}_{-156}	$1.41^{+0.01}_{-0.01}$	1.10	1.03
HIP 18544	PELS 86	3:58:01.72	20:40:35.5	$125.1^{+1.1}_{-1.1}$	6185^{+127}_{-102}	$2.24^{+0.03}_{-0.03}$	1.26	1.10
BD+23 455	PELS 121	3:27:42.07	23:48:12.4	$195.1^{+1.7}_{-1.7}$	5676^{+155}_{-111}	$2.58^{+0.03}_{-0.03}$	1.31	0.97
HIP 16753	PELS 124	3:35:31.73	22:49:24.0	$131.5^{+0.8}_{-0.8}$	6094^{+196}_{-135}	$1.64^{+0.01}_{-0.01}$	1.15	1.06
BD+26 592	PELS 128	3:39:53.74	26:43:00.3	$221.7^{+2.7}_{-2.6}$	5633^{+69}_{-101}	$3.40^{+0.06}_{-0.06}$	1.42	1.05
TYC 1256-516-1	PELS 135	3:45:01.68	19:33:32.8	$137.4^{+1.0}_{-1.0}$	6190^{+257}_{-167}	$2.67^{+0.03}_{-0.03}$	1.32	1.10
HIP 18091	PELS 146	3:52:00.83	19:35:47.8	$143.1^{+0.8}_{-0.8}$	5593^{+234}_{-205}	$1.16^{+0.01}_{-0.01}$	1.04	**1.43**
HD 23935	PELS 150	3:49:52.94	25:38:49.9	$138.5^{+0.8}_{-0.8}$	6008^{+163}_{-151}	$2.41^{+0.02}_{-0.02}$	1.28	**1.26**
BD+22 617C	PELS 173	4:00:53.14	23:11:37.5	$184.3^{+2.2}_{-2.2}$	6457^{+205}_{-112}	$3.95^{+0.06}_{-0.06}$	1.48	1.18
HIP 18955	PELS 174	4:03:44.20	22:56:38.5	$137.0^{+1.1}_{-1.1}$	5767^{+144}_{-266}	$2.20^{+0.02}_{-0.02}$	1.25	1.06
HIP 17316	TrS 42	3:42:24.03	21:28:23.6	$129.1^{+0.8}_{-0.8}$	5954^{+274}_{-148}	$1.62^{+0.01}_{-0.01}$	1.14	**1.10**
HD 24302	Tr 60	3:52:53.50	24:42:55.7	$140.5^{+1.2}_{-1.2}$	6376^{+181}_{-108}	$2.68^{+0.03}_{-0.03}$	1.32	1.01
H II 293	V* V1169 Tau	3:44:13.95	24:46:44.9	$136.1^{+1.0}_{-1.0}$	5503^{+145}_{-98}	$0.82^{+0.01}_{-0.01}$	0.94	0.98
H II 405	HD 23269	3:44:40.78	24:49:05.8	$134.5^{+1.0}_{-1.0}$	6072^{+68}_{-86}	$1.74^{+0.02}_{-0.02}$	1.17	0.98
H II 489	TYC 1803-808-1	3:44:56.40	24:25:57.4	$134.2^{+1.2}_{-1.2}$	5693^{+464}_{-189}	$1.06^{+0.01}_{-0.01}$	1.01	**1.20**
H II 571	TYC 1803-1156-1	3:45:15.39	25:17:21.2	$134.4^{+0.9}_{-0.9}$	5167^{+230}_{-127}	$0.57^{+0.01}_{-0.01}$	0.84	1.05
H II 727	V* V855 Tau	3:45:40.20	24:37:37.3	$131.6^{+1.1}_{-1.1}$	5927^{+156}_{-60}	$1.89^{+0.02}_{-0.02}$	1.19	1.00
H II 739	V* V969 Tau	3:45:42.15	24:54:20.7	$184.8^{+27.0}_{-20.9}$	5820^{+480}_{-170}	$4.40^{+0.58}_{-0.58}$	1.53	1.00
H II 923	BD+22 548	3:46:10.07	23:20:23.0	$122.5^{+0.9}_{-0.9}$	5775^{+67}_{-108}	$1.13^{+0.01}_{-0.01}$	1.03	1.06
H II 996	V* V1045 Tau	3:46:22.69	24:34:11.6	$138.7^{+0.9}_{-0.9}$	5775^{+317}_{-223}	$1.10^{+0.01}_{-0.01}$	1.02	**1.21**
H II 1117	HD 282975	3:46:37.73	23:47:15.0	$134.6^{+0.9}_{-0.9}$	5535^{+45}_{-116}	$1.34^{+0.01}_{-0.01}$	1.08	1.04
H II 1309	HD 23584	3:47:10.09	24:16:35.1	$136.1^{+1.2}_{-1.1}$	6165^{+175}_{-71}	$2.45^{+0.03}_{-0.03}$	1.29	0.97
H II 1338	HD 23608	3:47:16.59	24:07:41.5	$95.1^{+10.2}_{-8.4}$	6355^{+141}_{-105}	$2.34^{+0.24}_{-0.24}$	1.27	0.96
H II 1514	HD 282967	3:47:40.45	24:21:52.5	$136.2^{+1.2}_{-1.2}$	5629^{+75}_{-136}	$0.97^{+0.01}_{-0.01}$	0.98	1.07
H II 1613	HD 282973	3:47:52.51	23:56:28.4	$134.3^{+1.0}_{-1.0}$	6003^{+121}_{-95}	$1.68^{+0.02}_{-0.02}$	1.15	1.01
H II 1726	HD 23713	3:48:07.12	24:08:30.9	⋯	6444^{+455}_{-446}	⋯	⋯	1.04
H II 1797	BD+23 551	3:48:16.91	23:38:12.5	$140.4^{+0.9}_{-0.9}$	5886^{+84}_{-64}	$1.49^{+0.01}_{-0.01}$	1.11	**1.52**
H II 1856	HD 282971	3:48:26.20	24:02:53.5	$135.0^{+1.1}_{-1.1}$	5956^{+93}_{-103}	$1.49^{+0.02}_{-0.02}$	1.11	0.94
H II 1912	HD 23778	3:48:34.81	24:10:51.2	$221.4^{+66.8}_{-41.8}$	6256^{+365}_{-173}	$8.59^{+1.76}_{-1.76}$	1.86	0.97
H II 1924	Cl Melotte 22 1924	3:48:34.54	23:26:04.4	$136.8^{+0.9}_{-0.9}$	5741^{+177}_{-93}	$1.16^{+0.01}_{-0.01}$	1.04	1.04
H II 2027	Cl Melotte 22 2027	3:48:48.95	24:16:02.8	$143.0^{+1.0}_{-1.0}$	5066^{+363}_{-82}	$0.88^{+0.01}_{-0.01}$	0.96	0.97

Table 1
(Continued)

Name	Alternate Name	R.A. (J2000)	Decl (J2000)	Distance[a] (pc)	$T_{\rm eff}$[b] (K)	$L_{\rm star}$[b] ($L_\odot$)	$M_\star$ ($M_\odot$)	24 μm excess ratio[c]
H II 120	TYC 1799-102-1	3:43:31.98	23:40:25.7	$135.7^{+1.1}_{-1.0}$	5524^{+688}_{-94}	$0.78^{+0.01}_{-0.01}$	0.92	1.04
H II 152	V* V963 Tau	3:43:37.77	23:32:08.7	$136.0^{+1.0}_{-1.0}$	5502^{+161}_{-229}	$0.83^{+0.01}_{-0.01}$	0.94	**1.12**
H II 173	Cl Melotte 22 173	3:43:48.44	25:11:23.6	$130.4^{+1.6}_{-1.6}$	5206^{+305}_{-159}	$0.76^{+0.01}_{-0.01}$	0.91	1.00
H II 174	V* V1271 Tau	3:43:48.38	25:00:14.8	$136.3^{+1.0}_{-1.0}$	4991^{+60}_{-32}	$0.41^{+0.01}_{-0.01}$	0.76	0.99
H II 250	Cl Melotte 22 250	3:44:04.26	24:59:22.5	$129.8^{+1.1}_{-1.1}$	5518^{+166}_{-135}	$0.76^{+0.01}_{-0.01}$	0.91	**1.12**
H II 314	V* V1038 Tau	3:44:20.19	24:47:45.4	$134.2^{+0.9}_{-0.9}$	5431^{+87}_{-107}	$0.90^{+0.01}_{-0.01}$	0.96	1.02
H II 514	Cl Melotte 22 514	3:45:04.03	25:15:27.4	$135.3^{+0.9}_{-0.8}$	5516^{+398}_{-71}	$0.85^{+0.01}_{-0.01}$	0.95	**1.19**
H II 1015	HD 282952	3:46:27.37	25:08:07.1	$135.0^{+1.0}_{-1.0}$	5626^{+101}_{-117}	$0.95^{+0.01}_{-0.01}$	0.98	0.98
H II 1101	HD 282954	3:46:38.80	24:57:33.8	$136.3^{+1.0}_{-1.0}$	5900^{+206}_{-271}	$1.26^{+0.01}_{-0.01}$	1.06	**1.48**
H II 1182	BD+22 552	3:46:47.08	22:54:51.5	$138.5^{+1.0}_{-1.0}$	5590^{+264}_{-225}	$1.06^{+0.01}_{-0.01}$	1.01	1.03
H II 1200	BD+22 553	3:46:50.56	23:14:20.3	$153.2^{+1.6}_{-1.5}$	5946^{+94}_{-79}	$2.14^{+0.03}_{-0.03}$	1.24	**1.15**
H II 1776	HD 282958	3:48:17.72	25:02:51.4	$133.5^{+1.0}_{-1.0}$	5499^{+101}_{-107}	$0.69^{+0.01}_{-0.01}$	0.89	1.02
H II 2147	V* V1282 Tau	3:49:06.14	23:46:51.8	$138.2^{+1.0}_{-1.0}$	5305^{+738}_{-199}	$1.02^{+0.01}_{-0.01}$	1.00	1.00
H II 2278	HD 282960	3:49:25.75	24:56:14.5	⋯	5080^{+324}_{-81}	⋯	⋯	0.98
H II 2506	BD+22 574	3:49:56.52	23:13:06.2	$146.5^{+1.1}_{-1.1}$	5849^{+104}_{-92}	$1.42^{+0.01}_{-0.01}$	1.10	1.00
H II 2644	Cl Melotte 22 2644	3:50:20.90	24:28:00.3	$137.4^{+1.1}_{-1.0}$	5469^{+166}_{-62}	$0.63^{+0.01}_{-0.01}$	0.87	1.01
H II 2786	V* V1175 Tau	3:50:40.11	23:55:58.1	$139.1^{+1.2}_{-1.2}$	5852^{+199}_{-103}	$1.25^{+0.01}_{-0.01}$	1.06	0.99
H II 2881	V* V1176 Tau	3:50:54.32	23:50:05.6	$147.1^{+16.5}_{-13.5}$	4917^{+122}_{-57}	$0.63^{+0.07}_{-0.07}$	0.87	1.00
H II 3097	Cl Melotte 22 3097	3:51:40.48	24:58:58.6	$134.6^{+1.3}_{-1.3}$	5441^{+184}_{-143}	$0.74^{+0.01}_{-0.01}$	0.91	1.01
H II 3179	HD 24194	3:51:56.89	23:54:06.1	$133.1^{+1.1}_{-1.1}$	5845^{+144}_{-172}	$1.42^{+0.02}_{-0.02}$	1.10	1.00

Notes.
[a] Distances from Gaia DR2 catalog parallaxes (Gaia Collaboration et al. 2018) using the method of Bailer-Jones et al. (2018).
[b] Stellar luminosities and effective temperatures from the Gaia DR2 catalog (Gaia Collaboration et al. 2018).
[c] 24 μm excess ratio reported by Sierchio et al. (2010) except for H II 1776 that is reported by Carpenter et al. (2009); significant detections are indicated in bold.

Table 2
ALMA Observations Log

Date	Antennas	Baselines (m)	pwv (mm)	Passband	Phase
2019 December 12	43	15.0-313.7	1.0	J0423-0120	J0357+2319
2019 December 13	43	15.0-313.7	1.2	J0423-0120	J0357+2319
2019 December 14	44	15.0-313.7	2.8	J0423-0120	J0357+2319
2019 December 15	42	15.1-313.7	0.8	J0423-0120	J0357+2319
2019 December 16	43	15.1-313.7	0.8	J0423-0120	J0357+2319
2019 December 17	43	15.1-312.7	1.1	J0423-0120	J0357+2319
2019 December 18	42	15.1-312.7	1.0	J0423-0120	J0357+2319

can be expressed for blackbody emission simply as a function of dust temperature, stellar effective temperature, and dust-to-star flux ratio (e.g., Beichman et al. 2006; Greaves et al. 2009). The ring-like appearance of most debris disks supports the assumption of a single value for the dust temperature as a reasonable approximation, even as some debris disks sometimes do span a broad range of radii (e.g., Kalas et al. 2006). The fractional luminosity provides a proxy for the total cross-sectional area of dust. Figure 1 shows curves for the minimum detectable values of $L_{\rm dust}/L_{\rm star}$ for a typical Solar-type star in the Pleiades sample ($L_{star} = 1.8\,L_\odot$, $T_{eff} = 5825$ K) as a function of T_{dust} for (1) the Pleiades sample observed at 24 μm by Spitzer with flux density more than 10% in excess of the extrapolated photospheric flux density (32% detected; see Sierchio et al. 2010); (2) the subsample of 20 systems observed at 70 μm by Spitzer with $3 \times rms = 21$ mJy (no detections, Stauffer et al. 2005); (3) the small group of five systems observed from the 70 μm subsample at 1.2 mm with the IRAM 30 m telescope with $3 \times rms = 2.1$ mJy, which are the most sensitive millimeter observations to date (no detections; Roccatagliata et al. 2009); and (4) the 1.3 mm ALMA observations for $3 \times rms = 160\ \mu$Jy beam^{-1}, representative of the Pleiades sample (see Table 3, where the rms value for each target was determined by the noise statistics of the entire image), as well as an additional fall off as the largest belts become spatially resolved (see Section 3.1). The millimeter curves also account for steeper than blackbody spectra at these long wavelengths (see Section 4.2.2 for details). The ALMA detection limit expressed in fractional luminosity is $L_{\rm dust}/L_{\rm star} = 2 \times 10^{-4}$ for $T_{dust} = 50$ K. This limit is comparable to the Spitzer 24 μm threshold for similar values of T_{dust}, and substantially better for dust belts at lower temperatures.

2.4. Background Source Confusion

The Pleiades cluster shows a reflection nebula from a nearby dust cloud, and the presence of this dusty cloud has the potential to confuse searches for excess emission from stars in the cluster. For ALMA, the interferometer response strongly

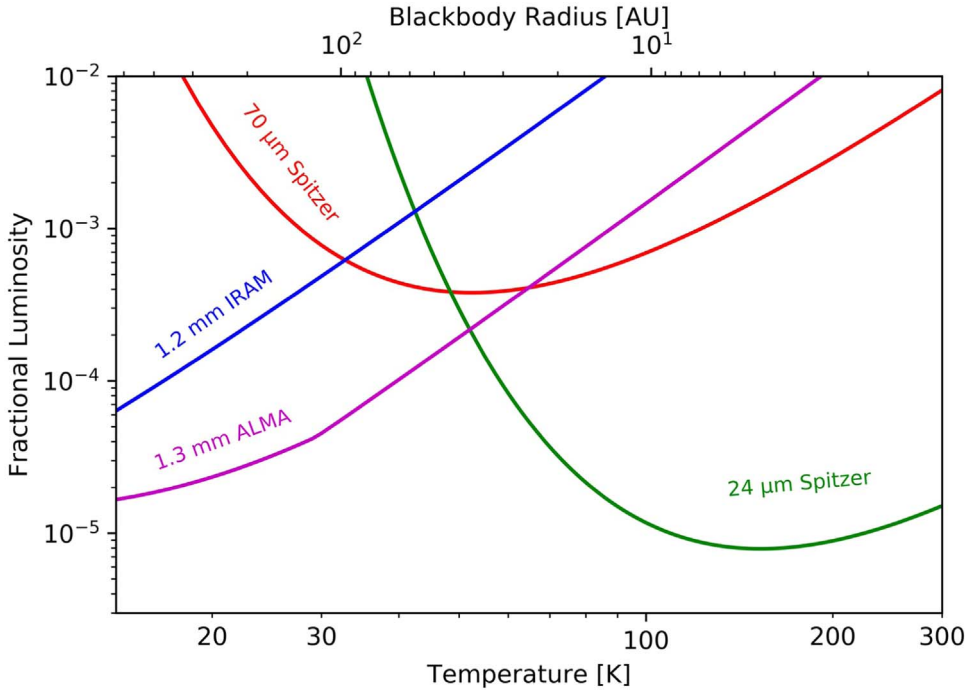

Figure 1. Detection limits for various debris disk surveys of Solar-type stars in the Pleiades, in terms of fractional luminosity ($L_{\rm dust}/L_{\rm star}$). The colored curves show the typical limits from the Spitzer 24 μm surveys of the Pleiades sample targeted for ALMA (green; Sierchio et al. 2010), the Spitzer 70 μm observations of a subsample of 20 systems (red; Stauffer et al. 2005), and IRAM 30 m 1.2 mm observations of 5 of those systems (blue; Roccatagliata et al. 2009). The purple line shows the ALMA detection limit, which improves on the millimeter sensitivity by about an order of magnitude (for more than an order of magnitude more systems).

spatially filters extended emission, so confusion from this cloud is unlikely to be problematic. Moreover, with a 1.″5 beam, extragalactic millimeter source counts show that chance alignments with background contaminants are insignificant (e.g., Carniani et al. 2015; González-López et al. 2020). The larger Spitzer beams at 24 μm (6″) and 70 μm (20″) clearly encompass any circumstellar dust emission around Pleiades members but also raise the specter of confusion with background sources. Stauffer et al. (2005) suggest that up to 2 out of 5 excess detections at 24 μm in their sample of 20 stars could be due to confusion with background Active Galactic Nuclei or Galactic cirrus.

3. Results

We used the `tclean` task in CASA to generate continuum images for each star in the sample. We adopted natural weighting to obtain the best point-source sensitivity, iterated to a threshold of 2 × the rms noise level, and applied a primary beam correction. Table 3 lists the beam size and rms noise for the image for each star, which ranges from 48 to 73 μJy beam^{-1}. The median rms noise was 54 μJy beam^{-1}. Figures 2 and 3 shows galleries of ALMA 1.3 mm images centered on each of the target stars in the full Pleiades sample.

3.1. Pleiades 1.3 mm Dust Continuum Emission Limits

We visually inspected the images and did not identify any significant sources of emission at the target star locations. We consider the ALMA detection limit to be 3× the rms noise level, an appropriate metric given that we have accurate a priori knowledge of the stellar positions. As an additional check, we fitted a point-source model to the visibilities for each target star using the `UVMultiFit` library (Martí-Vidal et al. 2014), restricting the fit source location to within 0.″2 offsets of the stellar position; this procedure also did not reveal any significant sources of emission.

We can translate the ALMA upper limits into estimates of dust mass by making standard assumptions, i.e., $M_{dust} = F_\nu d^2/(\kappa_\nu B_\nu(T_{dust})) \approx\ 0.012\ (F_{1.3\,mm}/54\ \mu Jy)(d/133.5\,pc)\ 2(T_{dust}/40\ K)\ M_\oplus$ where $F_{1.3mm}$ is the 1.3 mm flux density, $\kappa_{1.3mm} = 2.0$ cm^2 g^{-1} is the dust-mass opacity (Beckwith et al. 1990), and $B_\nu(T_{dust})$ is the Planck function taken to be in the Rayleigh–Jeans regime. We have adopted the dust-mass opacity for circumstellar disks advocated by Beckwith et al. (1990) in order to facilitate comparisons with other studies that make this common assumption. With this assumption, taking 3× the median rms noise level of the sample and $M_{dust} = 40$ K leads to a dust-mass limit of 0.036 $M_\oplus$ (about 3× the mass of the Moon). We also made a stacked image from the 76 continuum images, to obtain a deeper constraint on the average flux density of the undetected sources. This stacked image shows no significant emission at the center and has an rms noise level of 6.1 μJy beam^{-1}. Adopting the same assumptions leads to a dust-mass limit of 0.004 $M_\oplus$ for the mean level of dust around stars in this sample.

The typical FWHM beam size of 1.″5 (200 au) comfortably encompasses dust belts with radii up to 100 au. For larger dust belts, the emission spreads across multiple beams, and the sensitivity for detection is generally lower, depending in detail on the radius, width, and viewing geometry. To quantify the dust-belt detection threshold as a function of size in a simple way, we made a series of natural weight images with Gaussian tapers that increased in 0.″5 steps from 0 to 12.″5. This process produces a sequence of larger beams to cover larger dust belts (at any viewing geometry) at the cost of poorer point-source sensitivity. This sensitivity as a function of size scale has a similar shape for all of the targets because the u, v plane coverage of the ALMA observation is very similar. The sensitivity decreases by a factor of 2 at a beam size of 4.″4 and

Table 3
ALMA 1.3 Millimeter Imaging

Name	Beam FWHM (arcsec)	P.A. (deg)	rms Noise (μJy beam^{-1})
HIP 17317	1.56 × 1.42	0.8	48
BD+21 508	1.56 × 1.42	1.4	50
HD 23312	1.55 × 1.42	2.5	50
HD 24463[a]	1.62 × 1.41	10.6	58
HD 22627	1.60 × 1.41	−6.6	51
HIP 17044	1.60 × 1.41	−7.7	51
HD 23598	1.63 × 1.40	−0.8	53
HD 24086	1.63 × 1.40	0.3	51
HD 23975	1.62 × 1.40	−0.2	51
HD 22444	1.56 × 1.42	−12.7	51
TYC 1798-465-1	1.64 × 1.38	−26.6	57
HIP 16979	1.56 × 1.42	−14.4	49
HD 22680	1.58 × 1.42	−12.5	52
HIP 16639	1.62 × 1.40	−18.9	55
H II 25	1.61 × 1.40	−12.3	54
H II 102	1.58 × 1.42	−11.1	52
H II 1132	1.57 × 1.43	−9.1	50
H II 1139[a]	1.58 × 1.42	−9.1	55
H II 1766	1.63 × 1.39	−8.2	54
H II 2172	1.61 × 1.40	−9.0	52
H II 3031	1.60 × 1.41	−6.5	52
TYC 1802-95-1[a]	1.65 × 1.38	−17.2	59
HIP 17020	1.64 × 1.39	−19.5	50
HIP 17245	1.66 × 1.39	−16.7	54
HIP 17125	1.71 × 1.37	−12.5	55
BD+21 516	1.56 × 1.42	−18.8	49
HIP 18544	1.52 × 1.43	−3.1	50
BD+23 455	1.64 × 1.37	−27.2	54
HIP 16753	1.61 × 1.40	−25.6	52
BD+26 592[a]	1.68 × 1.38	−15.7	61
TYC 1256-516-1	1.52 × 1.41	−30.1	51
HIP 18091[a]	1.51 × 1.42	−27.3	73
HD 23935	1.65 × 1.39	−14.9	52
BD+22 617C	1.58 × 1.43	−7.6	50
HIP 18955	1.57 × 1.43	−5.1	53
HIP 17316	1.57 × 1.40	−27.6	52
HD 24302	1.63 × 1.40	−17.0	49
H II 293	1.64 × 1.38	−22.2	58
H II 405	1.63 × 1.38	−21.1	53
H II 489	1.63 × 1.38	−22.2	54
H II 571	1.64 × 1.38	−20.5	57
H II 727	1.63 × 1.38	−22.6	56
H II 739	1.64 × 1.38	−21.9	54
H II 923	1.61 × 1.41	−24.9	53
H II 996	1.66 × 1.35	−29.8	60
H II 1117	1.62 × 1.38	−25.0	52
H II 1309	1.63 × 1.38	−23.8	55
H II 1338	1.63 × 1.38	−24.7	54
H II 1514	1.63 × 1.38	−24.2	55
H II 1613	1.62 × 1.38	−25.4	55
H II 1726	1.63 × 1.37	−25.0	56
H II 1797	1.62 × 1.38	−26.6	52
H II 1856	1.63 × 1.38	−25.8	55
H II 1912	1.63 × 1.37	−25.6	52
H II 1924	1.62 × 1.39	−28.1	53
H II 2027	1.63 × 1.37	−26.0	54
H II 120	1.63 × 1.35	−31.4	56
H II 152	1.63 × 1.36	−31.9	53
H II 173	1.66 × 1.36	−25.8	58
H II 174	1.66 × 1.35	−27.9	56
H II 250	1.65 × 1.35	−28.3	55
H II 314	1.65 × 1.35	−28.4	55
H II 514	1.67 × 1.35	−28.4	57
H II 1015	1.66 × 1.35	−27.9	53
H II 1101	1.65 × 1.35	−28.2	57
H II 1182	1.64 × 1.39	−33.0	56
H II 1200	1.64 × 1.35	−35.0	56
H II 1776	1.66 × 1.35	−29.0	55
H II 2147	1.64 × 1.35	−32.3	56
H II 2278	1.67 × 1.35	−29.7	55
H II 2506	1.64 × 1.36	−33.6	55
H II 2644	1.66 × 1.35	−29.9	52
H II 2786	1.65 × 1.34	−31.9	57
H II 2881	1.65 × 1.34	−32.2	53
H II 3097	1.67 × 1.35	−29.9	54
H II 3179	1.65 × 1.34	−32.2	54

Note.
[a] Serendipitous emission source in the field of view.

a factor of 3 at 6.″9. While there is some dispersion in the noise levels at the largest tapers among the different targets, the increase in rms as a function of θ, the beam size FWHM (arcsec), is described well by the expression $1.000 + 0.32(\theta - 1.5) + 0.010(\theta - 1.5)^2$ for beam sizes in the range of interest. We will adopt this dependence of sensitivity with size scale in comparing the observations to population synthesis models in Section 4.2.

3.2. Serendipitous Source Detections

For five targets, we identified significant($>5\sigma$) sources of emission within the field of view but not associated with the centrally located star (HD 24463, H II 1139, TYC 1802-95-1, BD+26 592, and HIP 18091). For these serendipitous sources, we used `UVMultiFit` to fit a Gaussian model to the detected source(s), simultaneous with a central point source. Table 4 lists fitted offsets (east and north) from the field center, absolute coordinates, and flux densities. Figure 4 shows the images that contain these sources. The source in the field of TYC 1802-95-1 is clearly resolved. We checked the 2MASS infrared K band images of all of these sources for near-infrared counterparts and did not find any, although blending made the relevant region difficult to assess in some cases. The lack of any obvious near-infrared counterparts suggests the emission is not associated with stars located in the Pleiades cluster. Most likely they are dusty galaxies in the background. According to the 1.2 mm source counts of González-López et al. (2020), approximately five sources exceeding $\gtrsim 500\,\mu$Jy are expected across the sample ($\sim 5\sigma$ at the primary beam half power width), consistent with these detections.

4. Discussion

The ALMA 1.3 mm survey of a sample of FGK type stars in the 115 Myr old Pleiades cluster did not result in any detections of circumstellar dust emission. These data provide new limits on dust-belt fractional luminosities and masses in a regime of low temperatures and large radii that significantly improve on previous observations of Solar-type stars of Pleiades age. In particular, the dust-mass limit derived from stacking the nondetections is $<0.004\ M_\oplus$, about two orders of magnitude

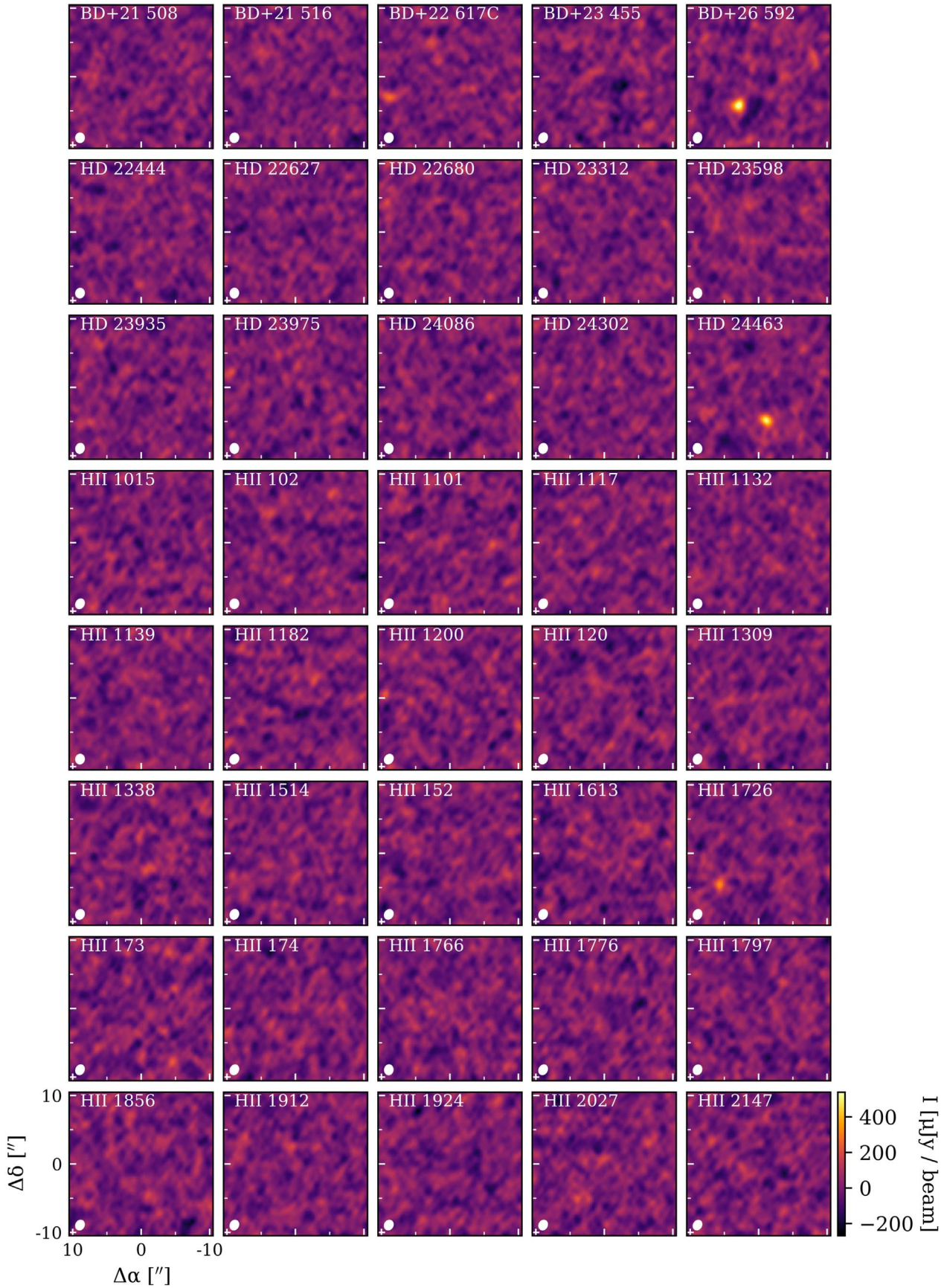

Figure 2. ALMA 1.3 mm images of the Pleiades FGK star sample, with typical at the origin of its panel. The synthesized beam is indicated by the ellipse in the lower left corner. No circumstellar dust emission is detected from any of the target stars.

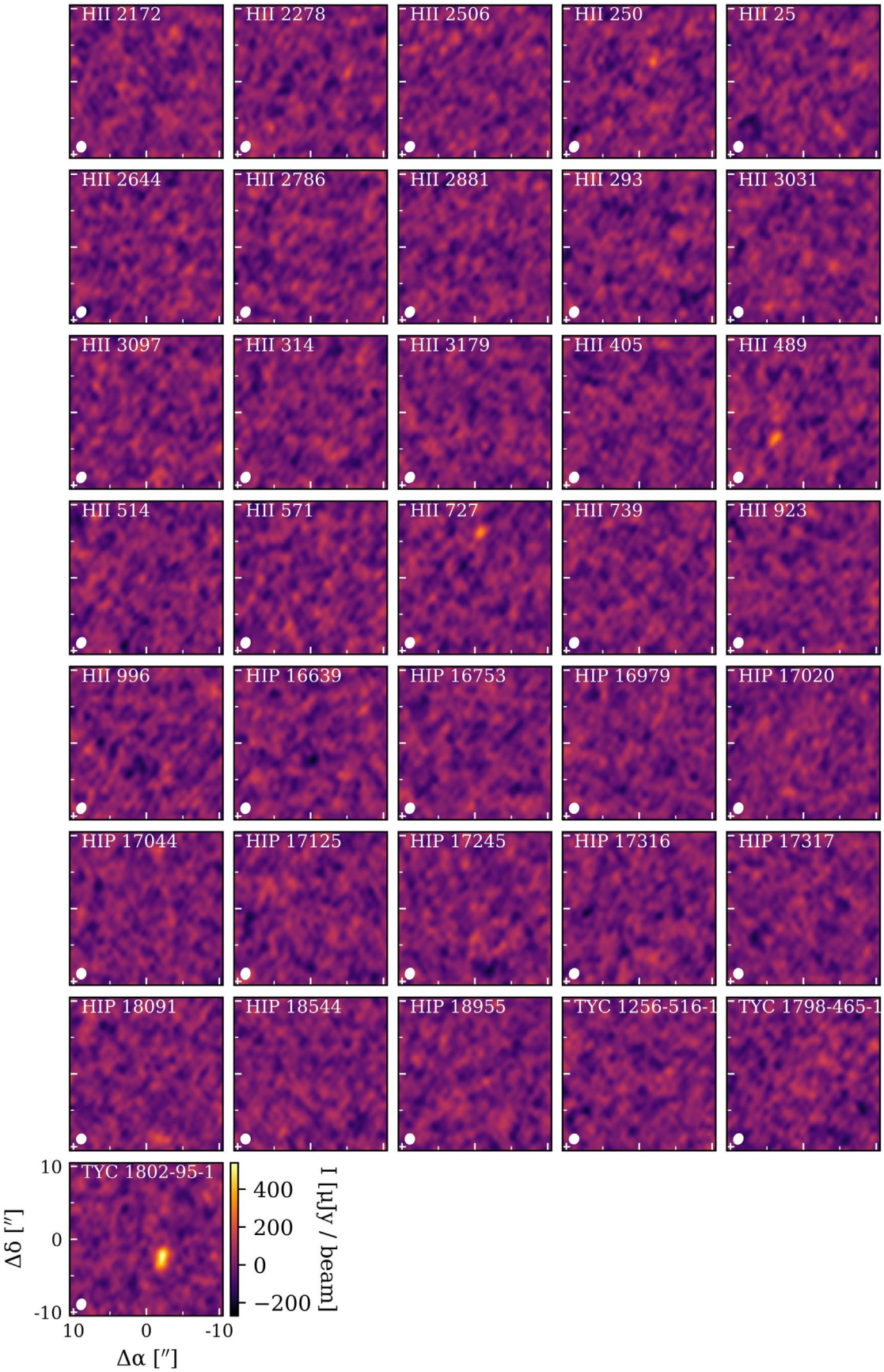

Figure 3. ALMA 1.3 mm images of the Pleiades FGK star sample (continued).

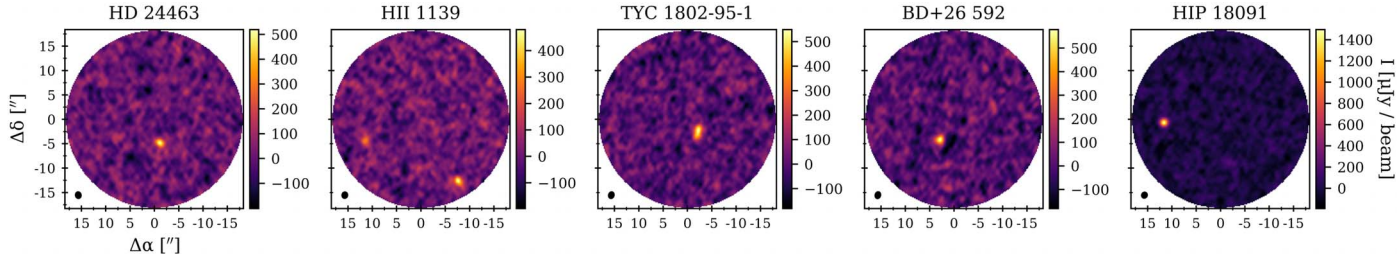

Figure 4. ALMA 1.3 mm continuum images for Pleiades fields where significant($>5\sigma$) emission sources were detected that are not associated with the target stars located at the field center. Table 4 lists the locations and flux densities of these sources. The beam sizes are indicated in the lower left corner of each panel.

Table 4
Serendipitous Source Detections[a]

Target Field	offset (E″, N″)	R.A. (J2000)	Decl (J2000)	Flux Density (mJy)
HD 24463	−1.1, −5.6	3:54:21.52	24:04:26.0	1.48 ± 0.22
H II 1139	−8.6, −13.1	3:46:39.43	23:06:23.2	1.84 ± 0.31
H II 1139	11.1, −4.4	3:46:40.74	23:06:31.9	1.38 ± 0.22
TYC 1802-95-1	−2.2, −2.3	3:34:47.05	26:05:38.0	1.25 ± 0.15
BD+26 592	3.0, −4.1	3:39:53.90	26:42:56.2	0.95 ± 0.11
HIP 18091	11.7, −0.6	3:52:01.57	19:35:47.2	2.58 ± 0.16

Note.
[a] Positions and flux densities obtained from Gaussian model fits to the visibilities and corrected for primary beam attenuation. The positional uncertainties are typically $<0\farcs2$ (1σ) in each coordinate.

lower than from previous millimeter observations of such stars in the Pleiades (for the same dust opacities and temperatures; Greaves et al. 2009; Roccatagliata et al. 2009). While a handful of Solar analogs believed to be at an age similar to the Pleiades are known to harbor massive ($\gtrsim$0.10 $M_\oplus$) dust belts at Kuiper Belt scales and beyond (Holland et al. 2017), such systems are evidently rare and not found in this Pleiades sample. For example, the disk around the nearby ∼80–200 Myr old G2 star HD 107146 would be 500 μJy at 1.3 mm at Pleiades distance (Williams et al. 2004; Ricci et al. 2015) and readily detected in this survey. We examine these Pleiades survey results in the context of debris disk evolution models based on collisional evolution.

4.1. Limits on Fractional Luminosity

As Figure 1 shows, these ALMA observations provide new sensitivity to dust belts with $T \lesssim 40$ K and fractional luminosity $>10^{-4}$. For warm disks with blackbody radii ∼5 au, the fractional luminosity limit implied by the observations is $f \sim 5 \times 10^{-3}$. For colder disks with blackbody radii ∼100 au, the fractional luminosity limit is $f \sim 5 \times 10^{-5}$. None of the Pleiades stars with significant 24 μm excess emission are detected at 1.3 mm. Given that these systems are also not detected by Spitzer at the shorter wavelength of 8 μm, the circumstellar dust must be at intermediate temperatures, and therefore concentrated at intermediate radii (from a few au to a few 10's of au). The previous nondetections of Pleiades targets at 70 μm and 1.2 mm are all consistent with the ALMA results (e.g., see Figure 1). The lack of 1.3 mm dust continuum emission detections implies an absence of massive and cold debris belts at large radial distances around the target stars.

4.2. Collisional Evolution Models

Multiwavelength observations of stars of different ages and spectral types provide constraints on debris disk incidence and fractional luminosity that have led to the development of various models to describe debris disk evolution based on collisions and "stirring" mechanisms that dynamically excite planetesimals leftover from the planet formation process (e.g., Wyatt & Dent 2002; Dominik & Decin 2003; Kenyon & Bromley 2004; Wyatt et al. 2007a).

Najita et al. (2022) used new coagulation models to assess the possibility that the observed population of cold debris disks around Sun-like stars evolve from the ∼25% of T Tauri systems that harbor large disks with ringed substructures. They show that the resulting "bright stalwart" debris disks by themselves can account for the available constraints on cold debris disk incidence and luminosities. In particular, models that start with rings at radii of 45 or 75 au with at least a few Earth masses in solids, using intermediate planetesimal formation efficiencies, readily produce cold belts with $L_{disk}/L_{star} \sim 10^{-3}$ at 10–100 Myr that subsequently fade. In this scenario, one would expect the ALMA 1.3 mm survey of the Pleiades to reveal many such belts. Since none were detected, the descendents of the large and ringed protoplanetary disks, if present, must be at least an order of magnitude less luminous at Pleiades age. These limits suggest different initial conditions or evolutionary pathways.

The analytical evolutionary model of Wyatt et al. (2007a), building on Wyatt & Dent (2002) and Dominik & Decin (2003), provides a practical framework for comparison with observations. In brief, this model assumes steady-state evolution in a catastrophic collisional cascade. Every star is assumed to be born with a planetesimal belt with radius r, narrow width dr, mass $M_{\rm disk}$, and a size distribution of colliding objects $n(D) \propto D^{2-3q}$, where $q = 11/6$ (i.e., collisional equilibrium; Dohnanyi 1969; Tanaka et al. 1996). In this analytical model, the belt properties are an initial condition; no physical explanation is provided for the origin of the belts. The production of dust is a top-down process that requires fragmentation of larger belt objects, and the evolution on long timescales is therefore determined by the collisional lifetime of the largest planetesimals, t_c (see equation 7 of Wyatt et al. 2007a). Then the time evolution of the disk mass is determined by the differential equation $dM_{tot}/dt = -M_{tot}/t_c$, which implies $M_{tot}(t) = M_{tot}(0)/[1 + t/t_c(0)]$, i.e., the debris disk mass (and fractional luminosity) decrease as t^{-1}. This is an approximation, as catastrophic collisions gradually reduce the size of the largest planetesimals over time, which results in a shorter collisional timescale and a faster decrease of disk mass (Kenyon & Bromley 2016). Nonetheless, this basic model has been successful in reproducing many observations of debris

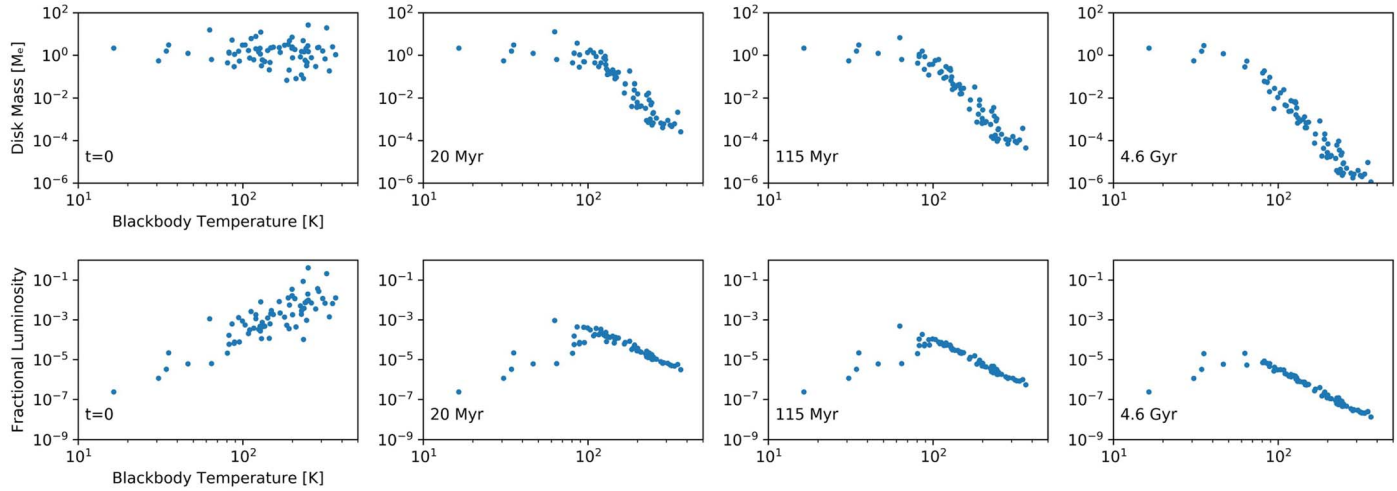

Figure 5. Top: belt masses plotted against blackbody temperature for an example population of simulated debris disks at four representative ages. The leftmost panel shows the initial masses, and subsequent panels show the belt masses after collisional evolution at 20 Myr, 115 Myr, and 4.6 Gyr. By 20 Myr, the warmest belts are already significantly depleted, while the coldest belts experience negligible mass depletion. Bottom: the fractional luminosities plotted against disk blackbody temperature for the same example population.

disks, including the properties of debris disks around A type stars of various ages at 24 and 70 μm (Wyatt et al. 2007b), the incidence and excess emission of nearby FGK type stars at 24, 70, 100, and 160 μm (Kains et al. 2011; Sibthorpe et al. 2018), and the (low) detection rate of debris disks around M stars (Morey & Lestrade 2014). Additional intuition about the time evolution behavior may be obtained by noting that $t_c \propto r^{3.5}/M_{tot}$ in this model, or $t_c \propto 1/(M_{tot}T^7)$ using blackbody radiative equilibrium to relate dust temperature to belt radius, i.e., $T \propto L_{star}^{1/4} r^{-1/2}$. The extremely steep dependence of timescale on dust temperature implies that warm (small radius) belts evolve much more rapidly than cold (large radius) belts.

4.2.1. Steady-State Evolution Parameters

We applied the collisional evolution model as described by Wyatt et al. (2007b) to the population of FGK stars in Pleiades observed by ALMA. The initial disk parameters are the disk mass $M_{tot}(0)$, the disk radius r and width dr, the material density ρ, maximum planetesimal diameter D_c, minimum dust grain diameter D_{bl}, and power-law index of the planetesimal size distribution, q. The time evolution is determined by the dispersal threshold Q_D^*, eccentricity e, and inclination i. We fix $dr = r/2$, $\rho = 2700\,\mathrm{kg\,m^{-3}}$, $q = 11/6$, and $e/i = 1$, following the analysis of nearby FGK stars by Kains et al. (2011). The disk masses are drawn from a log-normal distribution with mean $M_{\rm mid}$ and and width 1.14 dex (as determined by Andrews & Williams 2005), and the disk radii are drawn from a power-law distribution $N(r) \propto r^{\gamma}$ from 1 to 1000 au. The five free parameters in the model are $M_{\rm mid}$, γ, Q_D^*, e and D_c, and we set these to the values determined by Sibthorpe et al. (2018) from fitting to *Herschel* observations of debris disks around FGK stars near the Sun, i.e., $M_{mid} = 2.1\ M_{\oplus}$, $\gamma = -1.7$, $Q_D^* = 500$ J kg^{-1}, $e = 0.05$, and $D_c = 450$ km. With these assumptions, we can test if the same evolutionary model is consistent with observations of the Pleiades.The relevant stellar parameters in the models are luminosity, $L_{\rm star}$, mass, $M_{\rm star}$, and effective temperature, $T_{\rm eff}$. We adopted values for $T_{\rm eff}$, $L_{\rm star}$ and $M_{\rm star}$ from Table 1. (Highly accurate values for the stellar masses are not critical as the range across the sample is modest and model dependencies are weak.)

We omitted Pels 173 from our analysis for the same reasons it was excluded by Sierchio et al. (2010): the reddening to this star suggests it lies behind the Pleiades cluster and is not a member. We also omitted H II 1726 and H II 2278 because the Gaia DR2 catalog does not provide a set of stellar parameters.

4.2.2. Modified Blackbody Emission

To calculate the spectrum of each dust belt, we assumed modified blackbody emission and obtain the flux from $F_\nu = (2.95 \times 10^{10}) B_\nu(\lambda, T) f r^2 d^{-2} X_l^{-1}$ where F_ν is the disk's flux in units of Janskys, f is the fractional luminosity, r is the belt radius in au, d is distance to the star in parsecs, and X_l is an additional factor included to account for the steeper falloff due to departures from blackbody emission at long wavelengths, $X_l = (\lambda\ /\lambda_0)^{\beta}$, where λ_0 is a turnover wavelength (adopted to be 0.21 mm) and β is power-law index that reflects the dust emissivity(see Section 2.3 of Wyatt 2008). A value of $\beta = 1$ is often assumed for debris disks (e.g., Holland et al. 2017). However, detailed observations of the millimeter spectral slopes of nearby debris disks suggest that $\beta = 0.5$ provides a more appropriate empirical description (MacGregor et al. 2016). An additional effect is that the blackbody radius determined from radiative equilibrium tends to underestimate the true dust-belt radius since small grains do not emit efficiently at long wavelengths (e.g., Booth et al. 2013). This dependence acts to increase ALMA sensitivity to dust belts of larger radii.

4.2.3. Pleiades Sample Population Synthesis

We took random draws from the distributions of disk masses and radii to generate a population of belts around each of the 73 stars considered in the sample. These disks were then evolved to the Pleiades age of 115 Myr following collisional evolution, to produce a synthetic dust belt associated with each star. Then fluxes in the relevant bands were calculated for each one. This process was repeated 10,000 times to build up meaningful statistics.

Figure 5 illustrates the evolution of belt masses and fractional luminosities as a function of belt blackbody temperature for a single population of 73 stars at several ages.

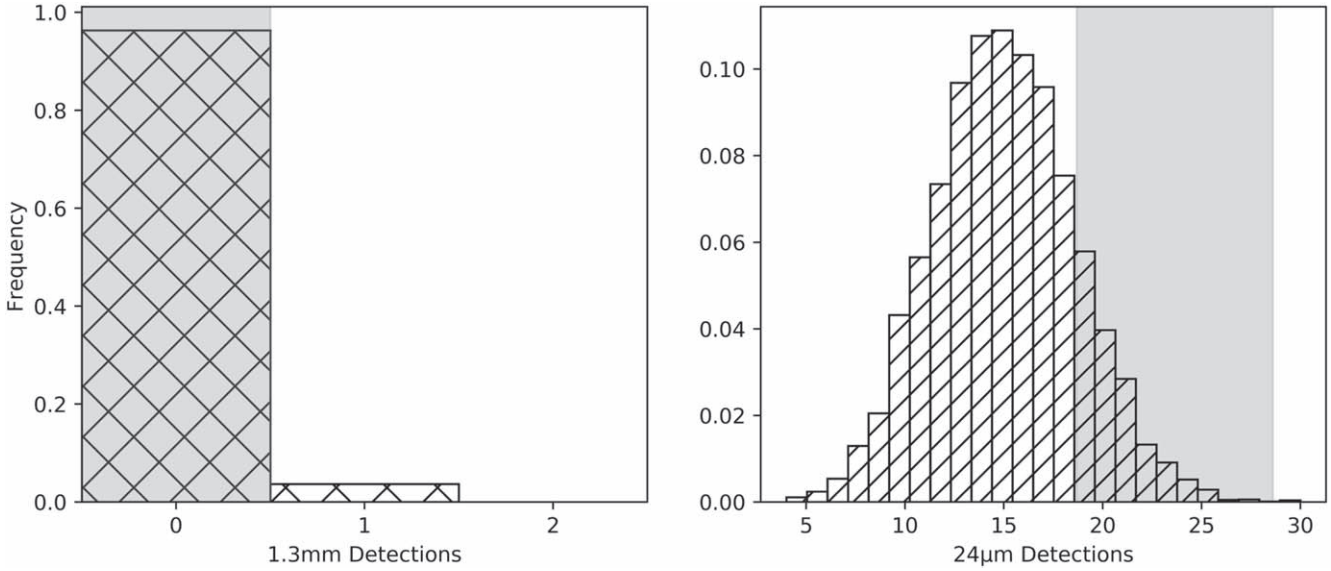

Figure 6. The hatched histograms show population synthesis models predictions for the detection frequency of debris disks in the Pleiades Solar-type star sample (left) by ALMA at 1.3 mm at the achieved sensitivity, and (right) by Spitzer at 24 μm, following the detection criterion of Sierchio et al. (2010). The gray shaded regions in each panel indicate the observed number (with associated uncertainties).

The initial disk masses arise from sampling the log-normal distribution. By 20 Myr, the warmest belts already have significantly depleted mass, due to the steep dependence on dust temperature of the collisional lifetime of the largest planetesimals. By contrast, the coldest belts ($T \lesssim 75K$) retain most of their mass at 20 Myr, at 115 Myr, and even on Gyr timescales. For a belt around a $1.0\,M_{\odot}$ star at 5 au radius, $t_c = 5.8/(M_{tot}/M_{\oplus})$ Myr, while for a belt at 50 au radius, $t_c = 8.8 \times 10^4/(M_{tot}/M_{\oplus})$ Myr and the initial mass is a dominant factor. This behavior is also reflected in the fractional luminosities. At late times, the fractional luminosity is strongly dependent on blackbody temperature (or radius) as the belts are collisionally depleted. The coldest belts are governed by very long collisional lifetimes.

Figure 6 (left panel) shows the frequency of 1.3 mm detections of dust belts for the sample of 73 Pleiades stars, given the sensitivity achieved in the ALMA survey. From the 10,000 realizations of this Pleiades sample, there are 9670 with zero detections (96.7%), 325 with one detection (3.25%), and five with two detections (0.05%). Thus the ALMA nondetection of any significant disk emission from the Pleiades sample is in agreement with the most likely outcome of these models. Much deeper integrations would be needed to detect a significant number of dust belts in this model population. Only about 5% of the targets have 1.3 mm flux densities that exceed 20 μJy, a level that would require almost an order of magnitude better sensitivity for detection (corresponding to $\sim$100 times longer integration times, or $\sim$7 hr on source with ALMA). This aspect of the modeled population is consistent with the flux density limit obtained from stacking the individual ALMA images of Pleiades stars.

The assumed long wavelength slope of the millimeter emission, encapsulated in the parameter β, has a modest impact on the 1.3 mm emission and the resulting detection statistics. In particular, a shallower unmodified blackbody spectrum ($\beta = 0$) extended (unrealistically) to the millimeter regime would result in at least one ALMA detection in 34% of the simulated populations. For the steeper $\beta = 1$, at least one ALMA detection from the sample would occur less than 1% of the time.

The population synthesis also provides predictions for 24 μm emission to compare with the Spitzer observations of the Pleiades sample. The 24 μm observations are much more sensitive than the 1.3 mm survey to the bulk of the dust belts. Sierchio et al. (2010) found significant excess emission from 23/71 stars, for a detection rate of 32% $\pm$ 6.8% of the sample (where an excess ratio > 1.1 was considered significant, i.e., exceeding 3σ). Figure 6 (right panel) shows the distribution of 24 μm detections for the 10,000 simulated populations. The mean of this distribution is 15.1, with standard deviation of 3.4, or 21% $\pm$ 4.7% of the sample (taking into account that two targets were dropped because they lack Gaia catalog stellar properties). Given the dispersion in the model prediction and the observational uncertainties, the population synthesis model predictions are consistent with the observations. The trend of the data to the high side of the model predictions may indicate a contribution from background confusion. As noted in Section 2.4, Stauffer et al. (2005) cautioned that 10% of their sample (2/20) may be contaminated by background 24 μm emission. If this same fraction were to hold for the full sample of Sierchio et al. (2010), then the number of stars with significant 24 μm dust-belt detections would be lower, conceivably 16/71, close to the population synthesis prediction. However, the difference between the nominal number of 24 μm detections and the model prediction is not statistically significant and should not be overinterpreted.

At 24 μm, the photospheric excess ratios predicted by the population synthesis models are always less than 2, even in the most extreme systems. From this perspective, the H II 1132 and HD 22680 systems are notable, with excess ratios of 17.44 and 3.79, respectively, reported by Sierchio et al. (2010). These values are much higher than any of the other dust belts in the sample and not expected in the passive, steady-state collisional evolution scenario at Pleiades age. The corresponding fractional luminosity for H II 1132, the largest outlier, is 1.9×10^{-3} (from Table 2 of Sierchio et al. 2010). If the radius of this belt is 5 au, then it falls below the ALMA detection

threshold at the sensitivity of our 1.3 mm survey (although it would have been readily detected at 70 μm were it included in the FEPS sample for observation at that wavelength). These systems are candidates of interest for deeper observations at longer wavelengths, to characterize their excess emission and to understand their physical nature. One intriguing possibility is that dynamical disturbances in the associated planetary systems have resulted in an epoch of unusually high dust production.

Given the absence of any ALMA detections, consistency of the observations with the population synthesis prediction is not especially constraining to the collisional evolution model. An implicit assumption that remains to be explored is whether or not progenitors of debris disks in star clusters like the Pleiades could be different than those for the field population near the Sun. The recent recognition of a high incidence of bright debris disks in F-type stars in the nearby 23 Myr old β Pictoris moving group compared with older moving groups and the field suggests a faster evolution than steady-state collisional evolution in the first $\sim$100 Myr, perhaps due to different initial disk properties or perhaps other factors, such as the influence of planets (Pawellek et al. 2021). Since most field stars are thought to form in groups with $<$100 members like the nearby moving groups (Adams & Myers 2001), it seems unlikely that initial conditions are responsible. By contrast, about 10% of stars form in dense open clusters like the Pleiades, where it is more plausible that birth environment could be important. Studies of protoplanetary disk properties in rich cluster environments, in particular the Orion Nebula Cluster, hint at different disk bulk properties than in more distributed star-forming regions like Taurus, in particular smaller sizes and lower masses in close proximity to the harsh radiation fields of O-type stars (e.g., Eisner et al. 2018). If birth environment is not responsible, then the consistency of the Pleiades results with the population synthesis models suggests that whatever process results in overbright disks at 23 Myr has ended by $\sim$100 Myr.

5. Conclusions

The 115 Myr old Pleiades cluster provides an important testbed for models of debris disk evolution. Of particular interest are Solar-type stars surrounded by possible analogs of the early Kuiper Belt. We used ALMA to survey 76 FGK type stars in the Pleiades at 1.3 mm to improve on previous observations at this long wavelength in both sensitivity and number to probe the presence of massive cold dust belts. These observations obtained a typical beam size $\sim$1.″5 (200 au) and a median rms noise 54 μJy, and they showed no significant detections of circumstellar dust. Several sources detected within the ALMA fields of view of the Pleiades stars are consistent with the expected background of dusty galaxies. For a dust belt at 40 K, the 3σ limit on 1.3 mm flux density corresponds to a fractional luminosity, $L_{\rm dust}/L_{\rm star} < 10^{-4}$. These sensitive 1.3 mm observations provide a testbed for debris disk evolutionary models for a population at an age where there are few existing constraints. A standard, passive collisional cascade model for steady-state evolution is statistically consistent with the ALMA 1.3 mm flux density limits, as well as previous detection statistics at 24 μm and shorter infrared wavelengths. The millimeter observations reveal no outliers from the model expectations, in particular no high fractional luminosity cold belts similar to those found around a few Solar-type stars in the local field population. Two of the Pleiades systems shows extreme 24 μm excess emission that suggest significant departures from steady-state evolution, perhaps resulting from dynamical disturbances involving planets.

This paper makes use of the following ALMA data: ADS/JAO.ALMA#2019.1.00251.S. ALMA is a partnership of ESO (representing its member states), NSF (USA), and NINS (Japan), together with NRC (Canada), MOST, ASIAA (Taiwan), and KASI (Republic of Korea), in cooperation with the Republic of Chile. The Joint ALMA Observatory is operated by ESO, AUI/NRAO and NAOJ. The National Radio Astronomy Observatory is a facility of the National Science Foundation operated under cooperative agreement by Associated Universities, Inc. D.S. thanks the Smithsonian Astrophysical Observatory for summer research support to carry out parts of this project. L.M. acknowledges funding from the European Unions Horizon 2020 research and innovation program under the Marie Sklodowska-Curie grant agreement No. 101031685. M.A.M. acknowledges the National Aeronautics and Space Administration under award number 19-ICAR19_2-0041. We thank Scott Kenyon and Qizhou Zhang for many valuable comments on an early version of the manuscript. We also thank Joan Najita for stimulating discussion.

Software: CASA (McMullin et al. 2007), UVMultiFit (Martí-Vidal et al. 2014), astropy (The Astropy Collaboration et al. 2013).

ORCID iDs

David J. Wilner https://orcid.org/0000-0003-1526-7587
Luca Matrà https://orcid.org/0000-0003-4705-3188
Mark C. Wyatt https://orcid.org/0000-0001-9064-5598
Sean M. Andrews https://orcid.org/0000-0003-2253-2270
Meredith A. MacGregor https://orcid.org/0000-0001-7891-8143
Brenda Matthews https://orcid.org/0000-0003-3017-9577

References

Adams, F. C., & Myers, P. C. 2001, ApJ, 553, 744
Andrews, S. M., & Williams, J. P. 2005, ApJ, 631, 1134
Asphaug, E. 2014, AREPS, 42, 551
Bailer-Jones, C. A. L., Rybizki, J., Fouesneau, M., Mantelet, G., & Andrae, R. 2018, AJ, 156, 58
Astropy Collaboration, Robitaille, Thomas P., Tollerud, Erik J., et al. 2013, A&A, 558, A33
Beckwith, S. V. W., Sargent, A. I., Chini, R. S., & Guesten, R. 1990, AJ, 99, 924
Beichman, C. A., Tanner, A., Bryden, G., et al. 2006, ApJ, 639, 1166
Booth, M., Kennedy, G., Sibthorpe, B., et al. 2013, MNRAS, 428, 1263
Booth, M., Wyatt, M. C., Morbidelli, A., Moro-Martín, A., & Levison, H. F. 2009, MNRAS, 399, 385
Gaia Collaboration, Brown, A. G. A., Vallenari, A., et al. 2018, A&A, 616, A1
Carniani, S., Maiolino, R., De Zotti, G., et al. 2015, A&A, 584, A78
Carpenter, J. M., Bouwman, J., Mamajek, E. E., et al. 2009, ApJS, 181, 197
Demircan, O., & Kahraman, G. 1991, Ap&SS, 181, 313
Dohnanyi, J. S. 1969, JGR, 74, 2531
Dominik, C., & Decin, G. 2003, ApJ, 598, 626
Eisner, J. A., Arce, H. G., Ballering, N. P., et al. 2018, ApJ, 860, 77
Gáspár, A., Rieke, G. H., Su, K. Y. L., et al. 2009, ApJ, 697, 1578
González-López, J., Novak, M., Decarli, R., et al. 2020, ApJ, 897, 91
Gorlova, N., Rieke, G. H., Muzerolle, J., et al. 2006, ApJ, 649, 1028
Greaves, J. S., Stauffer, J. R., Collier Cameron, A., Meyer, M. R., & Sheehan, C. K. W. 2009, MNRAS, 394, L36
Holland, W. S., Matthews, B. C., Kennedy, G. M., et al. 2017, MNRAS, 470, 3606

Hughes, A. M., Duchêne, G., & Matthews, B. C. 2018, ARA&A, 56, 541
Kains, N., Wyatt, M. C., & Greaves, J. S. 2011, MNRAS, 414, 2486
Kalas, P., Graham, J. R., Clampin, M. C., & Fitzgerald, M. P. 2006, ApJL, 637, L57
Kenyon, S. J., & Bromley, B. C. 2004, AJ, 127, 513
Kenyon, S. J., & Bromley, B. C. 2008, ApJS, 179, 451
Kenyon, S. J., & Bromley, B. C. 2016, ApJ, 817, 51
Morey, É., & Lestrade, J.-F. 2014, A&A, 565, A58
Lodieu, N., Pérez-Garrido, A., Smart, R. L., & Silvotti, R. 2019, A&A, 628, A66
Löhne, T., Krivov, A. V., & Rodmann, J. 2008, ApJ, 673, 1123
Lovell, J. B., Wyatt, M. C., Ansdell, M., et al. 2021, MNRAS, 500, 4878
MacGregor, M. A., Wilner, D. J., Chandler, C., et al. 2016, ApJ, 823, 79
Martí-Vidal, I., Vlemmings, W. H. T., Muller, S., & Casey, S. 2014, A&A, 563, A136
Matthews, B. C., Krivov, A. V., Wyatt, M. C., Bryden, G., & Eiroa, C. 2014, in Protostars and Planets VI, ed. H. Beuther et al. (Tucson, AZ: Univ. Arizona Press), 521
McMullin, J. P., Waters, B., Schiebel, D., Young, W., & Golap, K. 2007, in ASP Conf. Ser. 376, Astronomical Data Analysis Software and Systems XVI, ed. R. A. Shaw, F. Hill, & D. J. Bell (San Francisco, CA: ASP), 127
Melis, C., Reid, M. J., Mioduszewski, A. J., Stauffer, J. R., & Bower, G. C. 2014, Sci, 345, 1029
Najita, J. R., Kenyon, S. J., & Bromley, B. C. 2022, ApJ, 925, 45
Pawellek, N., Wyatt, M., Matrà, L., Kennedy, G., & Yelverton6, B. 2021, MNRAS, 502, 5390
Ricci, L., Maddison, S. T., Wilner, D., et al. 2015, ApJ, 813, 138
Rieke, G. H., Su, K. Y. L., Stansberry, J. A., et al. 2005, ApJ, 620, 1010
Roccatagliata, V., Henning, T., Wolf, S., et al. 2009, A&A, 497, 409
Sibthorpe, B., Kennedy, G. M., Wyatt, M. C., et al. 2018, MNRAS, 475, 3046
Sierchio, J. M., Rieke, G. H., Su, K. Y. L., et al. 2010, ApJ, 712, 1421
Stauffer, J. R., Rebull, L. M., Carpenter, J., et al. 2005, AJ, 130, 1834
Stauffer, J. R., Schultz, G., & Kirkpatrick, J. D. 1998, ApJL, 499, L199
Su, K. Y. L., Rieke, G. H., Stansberry, J. A., et al. 2006, ApJ, 653, 675
Tanaka, H., Inaba, S., & Nakazawa, K. 1996, Icar, 123, 450
Torres, G., Latham, D. W., & Quinn, S. N. 2021, ApJ, 921, 117
Williams, J. P., Najita, J., Liu, M. C., et al. 2004, ApJ, 604, 414
Wyatt, M. C. 2008, ARA&A, 46, 339
Wyatt, M. C., & Dent, W. R. F. 2002, MNRAS, 334, 589
Wyatt, M. C., Smith, R., Greaves, J. S., et al. 2007a, ApJ, 658, 569
Wyatt, M. C., Smith, R., Su, K. Y. L., et al. 2007b, ApJ, 663, 365
Zuckerman, B., & Becklin, E. E. 1993, ApJ, 414, 793